Highly conductive grain boundaries in cold-sintered barium zirconate-based proton conductors

Moritz Kindelmann[1,2,3,*], Sonia Escolastico[4], Laura Almar [4], Ashok Vayyala[1,2], Dylan Jennings[2,3], Wendelin Deibert[3], Wilhelm A. Meulenberg[3], Wolfgang Rheinheimer[3], Martin Bram[3], Jose M. Serra[4,*], Joachim Mayer[1,2], Olivier Guillon[3,5,*]

[1] RWTH Aachen University, Central Facility for Electron Microscopy (GFE), 52074 Aachen, Germany

[2] Forschungszentrum Jülich GmbH Ernst Ruska-Centre for Microscopy and Spectroscopy with Electrons (ER-C), 52425 Jülich, Germany

[3] Forschungszentrum Jülich GmbH, Institute of Energy and Climate Research, Materials Synthesis and Processing (IEK-1), 52425, Jülich, Germany

[4] Instituto de Tecnología Química, Universitat Politècnica de València-Consejo Superior de Investigaciones Científicas, 46022, Valencia, Spain

[5] Jülich Aachen Research Alliance, JARA-Energy, 52425, Jülich, Germany

Corresponding authors:

m.kindelmann@fz-juelich.de

jmserra@itq.upv.es

o.guillon@fz-juelich.de

Abstract

Proton-conducting barium zirconate ceramics have shown large potential for efficient electrochemical conversion and separation processes at intermediate operation temperatures. The high energy efficiency, robustness, and intermediate-temperature operation (500-650 °C) make proton-conducting cells promising candidates for future energy conversion systems. However, the major disadvantages of these materials are the inevitable high-sintering temperatures (>1500 °C),

leading to Ba-evaporation and formation of high-resistance grain boundaries, which dominate the electrochemical performance. Here, we introduce a novel processing route for proton-conducting barium zirconates, which, on the one hand, significantly lowers the maximum processing temperature and, on the other hand, overcomes the dominating influence of grain boundaries on total conductivity. The key step of this novel processing route is the cold sintering of the powder using pure water as a sintering aid to consolidate $BaZr_{0.7}Ce_{0.2}Y_{0.1}O_{3-\delta}$ (BZCY) at 350°C. We show that clean grain boundaries with a high acceptor-dopant concentration are preserved thanks to the recovery of the perovskite phase during thermal treatment at 1300 °C. This compensates the interfacial core charge, resulting in highly conductive grain boundaries, which do not limit the total conductivity. Consequently, dense BZCY electrolytes produced by our novel approach outperform the conductivity of conventionally sintered BZCY irrespective of the significantly lower maximum processing temperature and its nanocrystalline microstructure. Our presented approach opens up new possibilities for grain boundary engineering and might facilitate novel co-sintering pathways for barium zirconate-based components.

1. Introduction

Proton-conducting ceramics have immense potential for electrifying future energy systems based on renewable energy sources due to their reversible and robust performance in different operating modes [1]. Recent research shows the potential of proton-conducting fuel and electrolysis cells [2–7] and membrane reactors [8–12]. Most high-performance proton conductors are based on a solid solution of the perovskites $BaZrO_3$ and $BaCeO_3$ with Y as an acceptor dopant (BZCY) [13–15]. This material system allows adjusting the perovskite's stability and conduction properties to meet the operational requirements of specific applications. The $BaZrO_3$-rich composition

$BaZr_{0.7}Ce_{0.2}Y_{0.1}O_{3-\delta}$ (BZCY72) investigated here compromises sufficient proton conductivity and chemical robustness under different atmospheres [14,16,17].

The refractory nature of $BaZrO_3$-based perovskites requires processing temperatures of around 1600 °C to achieve sufficient densification. This is alleviated by using solid-state sintering with additives that enable a low-cost, single-step process called solid-state reactive sintering (SSRS) [18–20]. SSRS combines in situ phase formation and sintering promoted by transition metal oxides (NiO, CoO, or ZnO), leading to lower sintering temperatures (around 1500 °C) and enhanced grain growth for some BZCY compositions [21–23]. However, applying sintering aids leads to losing key conduction features, i.e., reduced proton uptake due to lower acceptor concentrations[24] and cationic segregation at grain boundaries [25].

Further reduction in processing temperatures is desirable but comes at the expense of fine-grained microstructures reducing the total proton conductivities [26], resulting in low conductivity due to the high resistance of their grain boundaries [27]. As with other perovskite ceramics, the grain boundaries of $BaZrO_3$ exhibit a positive core charge, leading to the formation of a negatively charged space charge layer (SCL) adjacent to the interface [28,29]. This redistribution of point defects leads to a blocking character of the grain boundary, hindering the transport of protons [30,31]. Additionally, segregation of acceptor dopants to the interface can be observed, leading to an enrichment in the grain boundary core and/or the SCZ [29,32,33]. This can partially compensate for the core charge, leading to an increase in grain boundary conductivity [34]. Proposed strategies to exploit this effect include high-temperature annealing, which allows redistribution of dopants, or incorporation of large A-side acceptor dopants [35]. Neither of these approaches has led to a sustainable and successful solution to simultaneously lower the sintering temperature and maintain sufficient grain boundary conductivity.

This study presents a novel processing route combining cold sintering and thermal post-treatments (TPT) to produce dense, Zr-rich BZCY electrolytes with highly conductive grain boundaries. Cold sintering is an emerging pressure- and liquid-assisted sintering process that enables significantly lower densification temperatures (below 400 °C) for a variety of ceramic materials (e.g., ZnO [36–38], $BaTiO_3$ [39,40], CeO_2 [41,42] and LLZO [43,44]) and composites [45–47]. Adapting hydrothermal processes found in geology, cold sintering applies these mechanisms to synthetic systems to enable low-temperature densification [48,49]. Here, we apply cold sintering to densify BZCY at 350 °C and 400 MPa using only deionized water as an additive, backed by the initial BZCY densification studies pinpointing the importance of precursors' phase composition[54].

Here, we now characterize the microstructure and phase formation during cold sintering at the macro- and nanoscale to elucidate the densification mechanisms. Under these sintering conditions, a high degree of densification can be achieved, but for electrochemical applications, a TPT (1300 °C for 10 h) is required to recover the target phase fully. To demonstrate the advantage of our approach compared to conventional processing, the grain boundary structure and chemistry of BZCY processed at low temperatures is characterized by high-resolution scanning transmission electron microscopy (STEM) and 3-dimensional atom probe tomography (3D-APT). In addition, electrochemical characterization by electrochemical impedance spectroscopy (EIS) and 4-point DC measurements confirms the high grain boundary conductivity. Our novel approach can overcome the incompatibility of fine microstructures and high protonic conductivity in barium zirconate ceramics by reforming the perovskite phase after densification. This allows acceptor dopants to segregate to the grain boundary and balance the core charge, significantly increasing the interfacial conductivity.

2. Experimental Methods

2.1. Powder synthesis and cold sintering

In the present study, ceramic powders with a nominal composition of $BaZr_{0.7}Ce_{0.2}Y_{0.1}O_{3-\delta}$ were used. The powder processing is based on a mixed oxide route and is optimized for solid-state reaction sintering (SSRS) [84], using 0.5 wt% NiO as a sintering aid. The powder precursors ($BaCO_3$, Y_2O_3, ZrO_2, and CeO_2 (all Sigma Aldrich, Germany) were dried, mixed, and pre-calcined at 1100 °C for 1 h. Afterward, the NiO (Sigma Aldrich, Germany) sintering aid was added, and the powders were wet milled for 24 h in isopropanol using zirconia balls and a jar. This starting powder was used for the conventionally processed samples. For cold sintering, an additional calcination step at 1300 °C for 5 h was introduced to adjust the pre-stage phase composition of the starting powder [54]. After calcination, the powder was milled for 30 min at 400 min^{-1} using a planetary ball mill (Retsch PM-400, Germany) with ethanol and 3 mm ZrO_2 milling balls in ZrO_2 milling jars. Afterward, the powders were dried at 80 °C in the air for 24 h and sieved through a 100 µm sieve to remove larger agglomerates. Before cold sintering, the powder had an average particle size (d_{50}) of 600 nm and was softly agglomerated.

The cold sintering experiments were carried out in a field-assisted sintering technology/spark plasma sintering machine (FAST/SPS, FCT Systeme HP-D5, Germany) with a TZM die set-up (TZM = Mo-based alloy from Plansee SE, Austria). The powders were pre-compacted in the die, and 5 wt% deionized water was homogeneously added to the green body using a micropipette (Eppendorf, Germany). The water/powder mixture was densified at a sintering temperature of 350 °C, with a uniaxial pressure of 400 MPa, a heating rate of 20 K/min, and a dwell time of 5 min. To derive the actual shrinkage from cold sintering experiments, the displacement curve was corrected for the thermal expansion of the mold assembly. After cold sintering, all samples were

subjected to thermal post-treatment (TPT) at different temperatures (1100, 1300, 1500, 1600°C) for 10 h in air to investigate the reformation of the perovskite phase.

Conventionally processed samples used for comparison were uniaxially pressed at 50 MPa and subsequently sintered in a powder bed of the same powder at 1600 °C for 5 h in air.

2.2. Density, phase analysis, and scanning electron microscopy

The relative density of the samples was evaluated through geometric measurements for cold sintered specimens (as they are unstable in contact with water) and Archimedes' method in water for thermally treated BZCY samples. The phase composition of the starting powders, cold sintered, and post-thermally treated samples was measured by X-ray diffraction (XRD, Brucker D4 Endeavor, USA). Additionally, the morphology of the powders and the microstructure of the sintered samples were characterized using scanning electron microscopy (SEM, Zeiss Ultra 55, Germany), and the grain sizes were determined by electron backscatter diffraction (EBSD, Oxford Instruments NordlysNano, United Kingdom).

2.3. Scanning transmission electron microscopy

To investigate the nanostructure of cold sintered samples as well as the chemical composition and structure at grain boundaries in cs1300-BZCY, electron transparent lamellae were cut using focused ion beam SEM (FIB-SEM, FEI Helios NanoLab 460F1, USA). After FIB preparation, Ar ion polishing (NanoMill, Fischione Instruments, USA) was used to improve sample quality for high-resolution imaging. Scanning transmission electron microscopy (STEM) was performed at 200 kV using a Cs-corrected Hitachi HF5000 microscope (Hitachi High-Tech, Japan) equipped with energy-dispersive X-ray spectroscopy (EDS) detector system (Advanced EDX System Ultrim TLE, Oxford Instruments, United Kingdom). EDS analysis was done using Hyperspy. The low

magnification EDS data was quantified (Figure 2a) using a standard less (Cliff-Lorimer) method to remove thickness effects from the map.

2.4. Atom probe tomography

To investigate the grain boundary chemistry of cs1300 BZCY, nanoneedle specimens were prepared using a Helios Nanolab 650i dual beam focused ion beam (FIB) (Thermo Fisher Scientific, USA) tool. APT measurements were conducted using a LEAP 400X HR instrument (Ametek Inc., USA) operating in laser mode with a laser pulse energy range of 10-30pJ, a laser pulse frequency of 200kHz, and a detection rate of 0.01 ions per pulse (1%). The base specimen temperature for all the measurements was maintained at cryogenic temperature (20K). Reconstruction and analysis of the APT data were performed using the Integrated Visualization and Analysis Software (IVAS) package 3.6.14 software. Reconstruction parameters were carefully determined, including an image compression factor (ICF) set to 1.5 (based on the measured evaporation length of the sample after the APT-run), a field factor of 3.3, and an evaporation field (F) set to 17 V/nm (based on the final radius (post-APT measurement) of the apex). The deconvolution of peak overlaps in mass spectra was also performed for accurate bulk compositional analysis.

2.5. Electrochemical characterization

The electrochemical performance of the developed samples is evaluated by DC-conductivity measurements and electrochemical impedance spectroscopy (EIS).

Total conductivity was measured on sintered bars by the standard four-point DC technique. Rectangular bars used in conductivity measurements were obtained by polishing the disk samples from cold sintering and conventional manufacturing techniques. Silver paste and wires were used

for contacting. The constant current was supplied by a programmable current source (Keithley 2601), while the voltage drop was detected by a multimeter (Keithley 3706, both Keithley Instruments, USA). Total conductivity measurements were performed in different atmospheres, and the isotopic effect was evaluated. The employed atmospheres were: (1) wet 5% H_2 in Ar and 5% D_2 in Ar (where wet means 2.5% H_2O and 2.5% D_2O, respectively).

EIS analysis was conducted with a Solartron Analytical 1470E CellTest System frequency response analyzer (Ametek Inc., USA) in the 0.03-10^6 Hz frequency range. The disk samples were placed in a quartz reactor with Ag paste painted contacts and between Pt meshes, tested in a temperature range between 800 ºC and 500 ºC and humidified (3% H_2O) atmospheres: (a) synthetic air, (b) Ar and (c) 5% H_2-95% Ar with a total flow rate of 50 $mL \cdot min^{-1}$ at each sample side. The collected impedance data was analyzed and fit using the ZView software.

3. Results and Discussion

3.1. Microstructure and phase formation during cold sintering of BZCY

The phase formation and microstructure development during cold sintering and TPT was investigated in broad detail to understand the origin of the improved grain boundary properties, which lead to high proton conductivities despite the low overall processing temperatures and the nanocrystalline microstructures obtained. Throughout this study, three different sintering processes are discussed: cold sintered BZCY (CS), two-step processed BZCY – a combination of cold sintering and TPT – (TPT1300, for a TPT at 1300 °C) and conventionally sintered BZCY (CONV).

The two-step processing applied in this study is displayed in a schematic process scheme in Fig. 1a. First, the powders are filled into a metal pressing die, and deionized water is added. Then, cold sintering is performed at 350 °C using a uniaxial pressure of 400 MPa for 5 min in an instrumented field-assisted sintering/spark plasma sintering device (FAST/SPS). The total processing time for densification did not exceed 30 min. After cold sintering, the samples are removed from the pressing die and subjected to a TPT at 1300 °C for 10 h to reform the perovskite phase fully.

The shrinkage curve (corrected for instrument and tool elasticity, 1b) shows that a clear acceleration of the densification under high uniaxial pressures starts at around 100 °C when water starts to evaporate (increase in SPS chamber pressure, orange curve). The densification during cold sintering may involve particle rearrangement, particle surface cleaning, local dissolution, subsequent reprecipitation processes, and dislocation-based plastic deformation [48,50,51]. In BZCY ceramics, this process starts below the evaporation temperature of the water and continues up to 350 °C.

A scanning electron microscopy (SEM) image of a fracture surface of cs-BZCY is displayed in 1c, revealing the fine-grained microstructure and high relative density. However, X-ray diffraction (XRD) results (1e) suggest that parts of the powder decompose during cold sintering, forming several secondary phases ($Ba(OH)_2$, $BaCO_3$, and CeO_2). This behavior is caused by the instability of Ce-rich BZCY compositions, which are prone to decomposition under water/steam environments [52,53]. Here, we intentionally used a starting powder that consists of two perovskite phases (1e, blue diffractogram), one being a Ce-rich and the other a Zr-rich BZCY. This approach allows for controlling the dissolution behavior, enabling densification at low temperatures. Details on the impact of the composition of the starting powder were reported elsewhere [54].

To understand the densification behavior during cold sintering, we examined the sintering process in detail. In the first step, the Ce-rich BZCY reacts under cold sintering conditions with water and forms $Ba(OH)_2$, Y doped-CeO_2, and the residual, stable perovskite $BaZr_{1-x}Y_xO_3$. In the second step, the formed $Ba(OH)_2$ either solves in residual H_2O or reacts with carbon-containing molecules (CO, CO_2, or carbon tape used during sintering) to form $BaCO_3$ and H_2O. All of these phases could be detected using XRD.

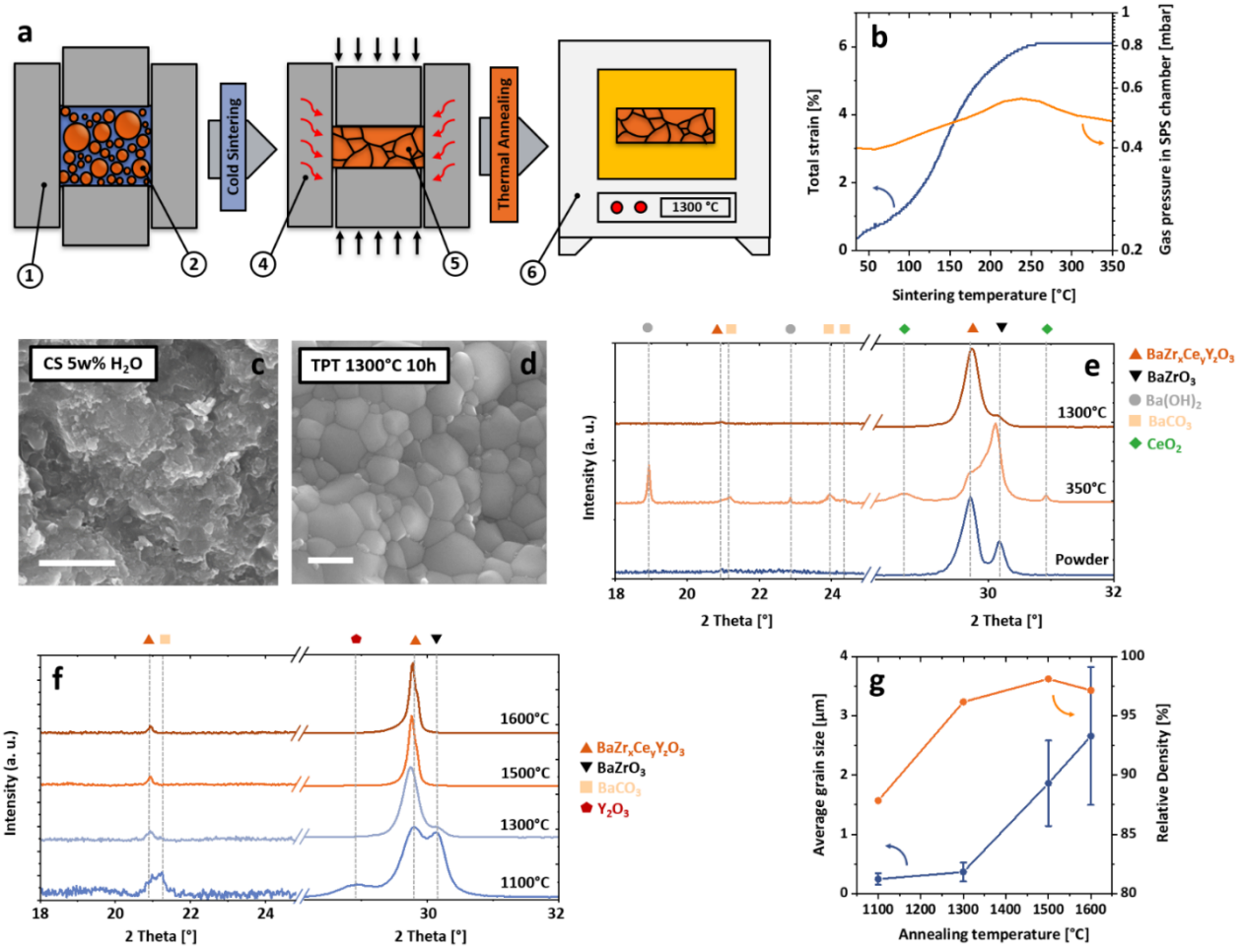

Figure 1: Processing, microstructure development, and phase evolution of cold sintered BZCY. (a) Schematic representation of the processing route: (1) Molybdenum tool (TZM) tool, (2) BZCY powder/water mixture, (3) applied mechanical pressure, (4) Joule heating during cold sintering, (5) densified sample, (6) TPT in a box furnace. (b) Total strain calculated from relative punch

displacement during cold sintering of BZCY powders and the associated gas pressure curve highlighting the evaporation process of H_2O. (c, d) SEM micrographs of BZCY fractured surfaces of cold sintered (CS) (350 °C, 400 MPa, 10 min, 5% H_2O) and thermally treated (TPT) (1300 °C, 10 h). Scale bar 500 nm. (e) XRD diffractograms showing the BZCY phase evolution from powder, cold sintered state to thermal post-treated (1300 °C, 10 h). (f) Phase evolution after different thermal post-treatments (from 1100 °C to 1600 °C), highlighting the reformation of the target BZCY phase after TPT. (g) Relative density and average grain size after the different thermal post-treatments.

The secondary phases forming during cold sintering have a low strength (especially $BaCO_3$ [55]), easing particle rotation and sliding under high mechanical pressures enabling densification. However, residual secondary phases prevent electrochemical testing of the cold-sintered BZCY under application conditions (wet atmospheres at temperatures from 400 to 800 °C). Therefore, a systematic variation of TPT (from 1100 to 1600 °C for 10 h in air) was conducted to investigate the reformation of the target phase and the associated microstructural development. Fig. 1f and 1g show the phase changes, the relative density, and the average grain size of samples annealed at different temperatures after cold sintering.

A TPT at 1100 °C is insufficient to reform the target phase, leaving two $BaZrO_3$ compositions and residual $BaCO_3$ and Y_2O_3 in the sample. In contrast, annealing treatments at 1300 °C and above result in a single BZCY phase with only minor residuals of $BaZrO_3$. Through a careful thermal decomposition of $BaCO_3$ above 1200 °C [56] and the dissolution of Y_2O_3 and CeO_2 into the perovskite structure, it is possible to produce dense (rel. density 96 %) and fine-grained BZCY polycrystals (average grain size of 365 nm). The microstructure of such a BZCY ceramic annealed at 1300 °C is displayed in Fig. 1d. Increased annealing temperatures at 1500 and 1600 °C led to coarser microstructures with grain sizes of 1.9 and 2.7 µm, respectively. The microstructure and

phase evolution were additionally investigated by SEM and HT-XRD, as shown in supplementary Fig. S1-S3.

To further understand the mechanisms that enable low-temperature consolidation through cold sintering, the microstructure and chemical composition were investigated by STEM-EDS. The multi-phase microstructure observed by XRD is resolved at a high spatial resolution. Fig. 2a shows an overview and its associated EDS mappings. Three different phases can be differentiated as highlighted: (I) a Zr-depleted and C-rich phase, which can be assigned to $BaCO_3$, (II) Ce and Y-rich nanoparticles, and (III) a Zr-rich matrix with a homogeneous composition. Additionally, high-resolution STEM imaging confirms that Y and Ce-rich nanoparticles (Fig. 2b, c) are cubic CeO_2 particles with a high amount of Y. The lattice spacing was measured (3.24 Å) in 2c, which makes it possible to derive the visible lattice plane (111) in the cubic crystal structure of CeO_2. Furthermore, a high-resolution EDS mapping (2d) confirms the chemical composition and reveals that precipitated CeO_2 particles are embedded into a $BaCO_3$ matrix. However, the high electron-beam sensitivity of the carbonate matrix complicates conventional spectral imaging leading to a comparably low EDS signal for Ba.

Combining the findings of the macroscopic phase and microstructure analysis (Fig. 1) with the high-resolution STEM investigation of cs-BZCY (Fig. 2) allows us to elaborate on the mechanisms enabling cold sintering of BZCY.

In BZCY, the densification mechanism during cold sintering can be divided into two stages, as schematically displayed in Fig. 2e. First, the dissolution of Ce-rich components, which can be affected by the applied pressure, and the associated formation of reaction products $Ba(OH)_2$ and $BaCO_3$. After the evaporation of water from the powder compact, these residuals remain in the

microstructure. Second, the pressure-assisted densification mechanism takes place, which is characterized by the stress exponent (51), generally determined by systematically varying the applied pressure. We assume that under the high uniaxial pressure applied during cold sintering, the low shear strength of the precipitated phases allows grain sliding and rotation mechanisms. Third, removing the residual phases and reincorporating Ce and Y back in the perovskite using TPT at elevated temperatures yields stable low-temperature processed BZCY ceramics.

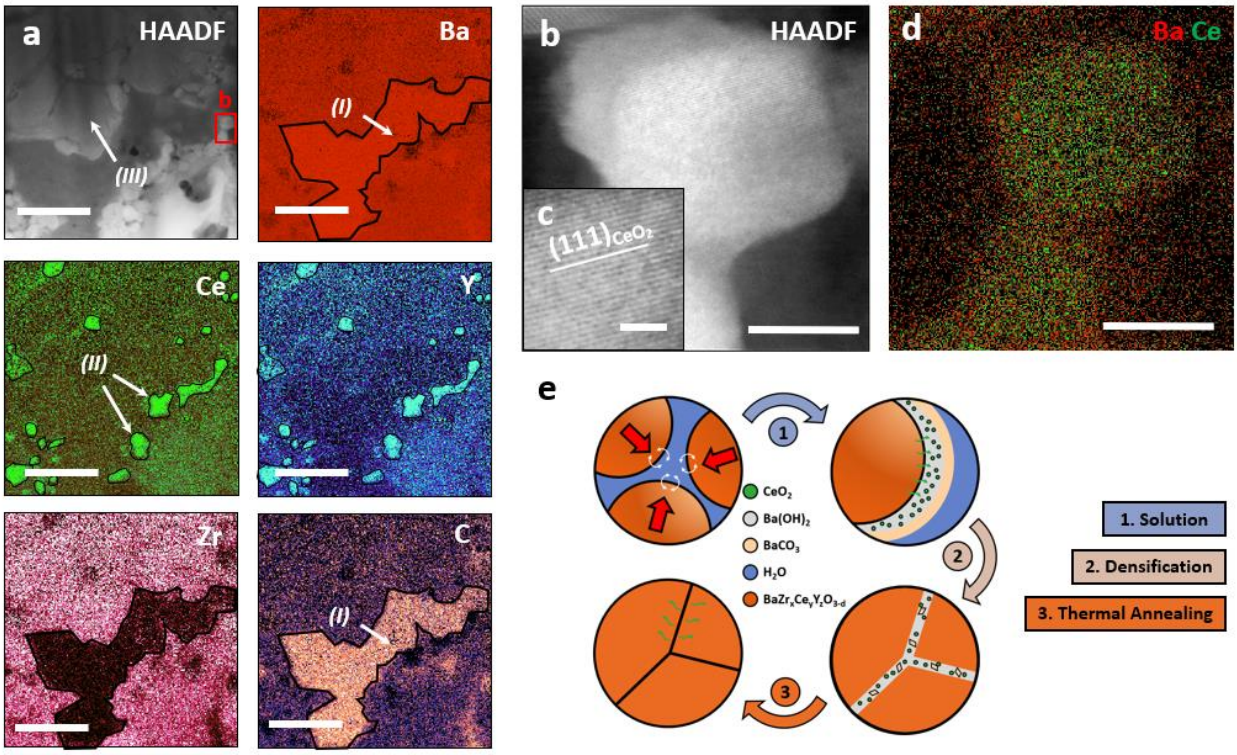

Figure 2: Nanostructure and chemical composition of cold sintered BZCY ceramics. (a) STEM-EDS overview of the microstructure and the chemical composition after cold sintering revealing secondary phases formed during processing. Scale bar 100 nm. (b) STEM detail image of a Ce and Y-rich nanoparticle marked in the overview image (a). Scale bar 10 nm. (c) Increased magnification of the lattice structure of the CeO_2 nanoparticle showing the (111) planes of CeO_2. Scale bar inlay 2 nm. (d) Combined EDS elemental map of Ba and Ce. Scale bar 10 nm. (e) Schematic sketch of the possible densification steps of cold sintering in BZCY ceramics: (1) Solution and reprecipitation (2) Pressure-assisted densification (3) BZCY phase reformation through TPT.

3.2. Electrochemical performance of low-temperature processed BZCY ceramics

The electrochemical performance of low-temperature processed BZCY electrolytes was determined by electrochemical impedance spectroscopy (EIS) in three different atmospheres (i.e., wet (3% H_2O) air, wet Ar, and wet H_2) (Fig. 3a-c) and compared to results derived from DC conductivity measurements under wet reducing conditions (wet H_2 Fig. 3d). We verified that similar values were obtained, revealing a significantly higher conductivity of TPT1300 compared to its conventionally processed counterpart.

In Fig. 3a-c, the bulk and the grain-boundary conductivities obtained after impedance analysis for the low-temperature processed BZCY (1300 °C, 10 h) are directly compared with a conventional SSRS sample (1600 °C, 5 h, details can be found in the supplementary information). The TPT1300 electrolytes revealed superior proton-conduction properties compared to samples produced by SSRS in all tested atmospheres (additionally corroborated by EIS measurements on the TPT1500 sample, figure S4). Bulk conductivities are in the same range in wet Ar and H_2. Remarkably, the grain-boundary conductivity in low-temperature processed BZCY is not limiting the overall conductivity despite its nanocrystalline microstructure. This behavior directly contrasts the conventionally sintered sample and observations made for $BaZrO_3$-based proton conductors in general [30,57,58], which exhibit a high grain boundary resistivity. Additionally, the differences in activation energy for grain boundary conductivity point towards a change in the proton-transport mechanism across the grain boundaries.

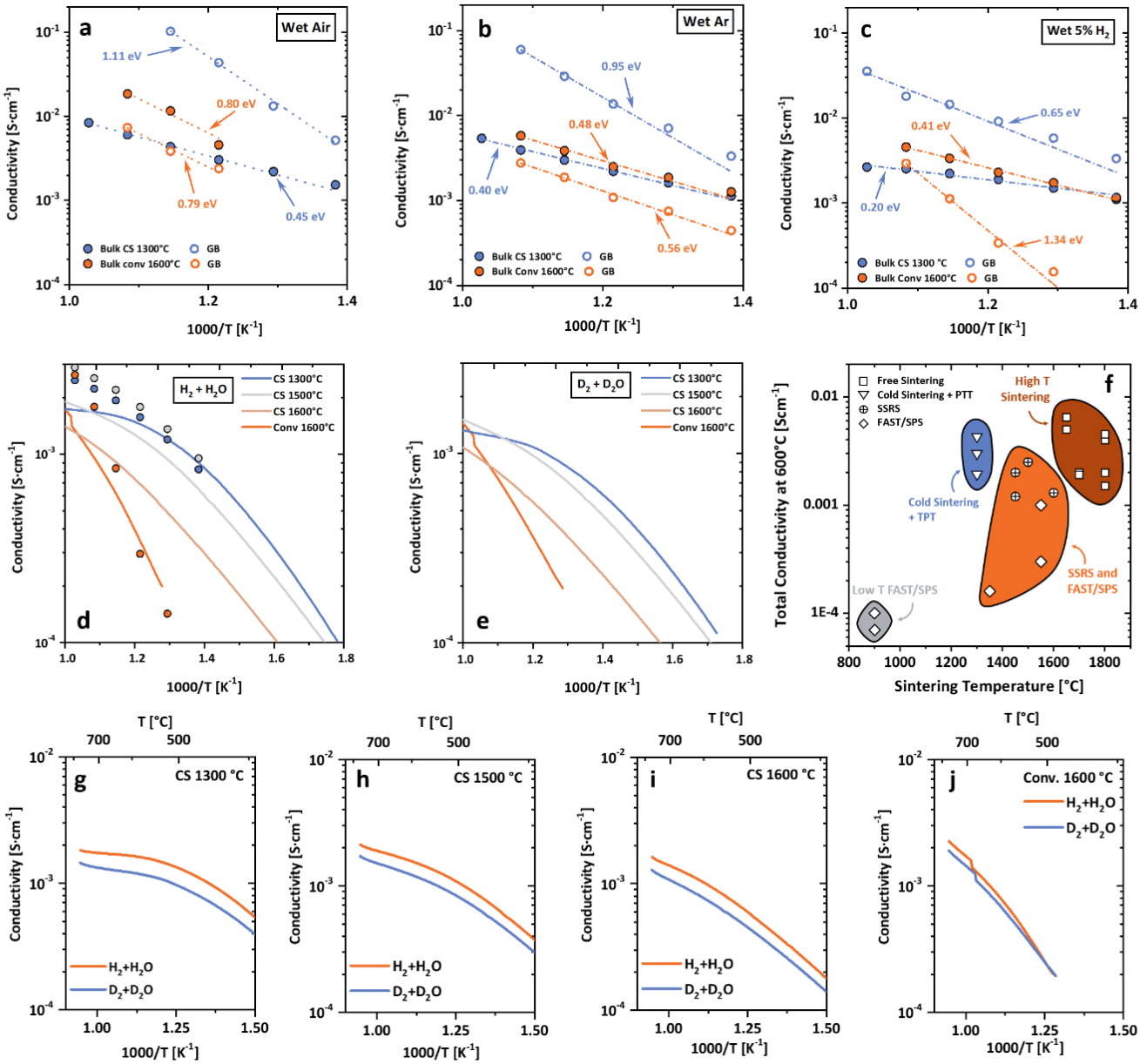

Figure 3: Electrochemical properties of low-temperature processed BZCY. Electrochemical impedance spectroscopy (EIS) of CONV (1600 °C, 5 h) and TPT1300 (1300 °C, 10 h) BCZY in wet air (a), wet Ar (b), and wet H_2 (c) (3% H_2O). Full circles represent bulk conductivity, and empty circles represent grain boundary conductivity. (d) Total conductivity determined by DC conductivity measurements in a reducing atmosphere (wet 5% H_2). Filled circles represent the corresponding EIS measurements. (e) DC measurements using D_2 in D_2O revealing the isotopic effect and highlighting the high protonic conductivity of low-temperature processed BZCY. (f) Literature overview of the total conductivity data at 600 °C as a function of processing temperature summarizing different sintering approaches and material systems [14,22,23,61–66]. The material compositions and experimental details are displayed in Table S1 and highlighted in Fig S6. (g-j) H_2/D_2 isotopic effect for cold sintered samples after different TPT from 1300 to 1600 °C and CONV, respectively.

From the H_2/D_2 isotope effect (Fig. 3g-j) observed in reducing atmospheres, it can be concluded that the improvement in transport properties is clearly due to the enhanced proton transport through the nanocrystalline microstructure in TPT1300 [15,59,60] (additional measurements in Ar/H_2 and ArD_2 which also show high protonic mobility in TPT1300 are shown in Fig. S5). The total conductivity reported here is the highest for Zr-rich BZCY compositions at these low overall sintering temperatures, highlighted using an overview graph summarizing total conductivities at 600 °C from different literature sources [14,22,23,61–66] (Fig. 3f).

3.3. Probing the interfacial structure and chemistry of low-temperature processed BZCY

The electrochemical performance of proton-conducting perovskites is highly dependent on the properties of their grain boundaries [67]. Therefore, a thorough investigation of the interfacial structure and chemistry of low-temperature processed BZCY is necessary. We utilized various STEM techniques and APT to characterize grain boundaries of TPT1300 and their difference from conventionally processed samples (CONV).

The chemical composition of grain boundaries of both sample types was investigated using STEM-EDS and is depicted in Fig. 4a and 4b. Both grain boundaries are imaged in an edge-on state (i. e. the grain boundary plane is parallel to the electron beam) to avoid overlap and unwanted broadening of the spectral image at the interface. Clear differences between the grain boundaries can already be seen in the bright field (BF) images of the two samples. The TPT1300 sample shows a thin and clean interface (thickness of about 0.6 nm), while the conventionally processed samples show a structurally different interlayer (thickness of about 2.1 nm). This observation is confirmed by elemental mapping of the two-grain boundaries. In TPT1300, Y and Ni segregate on the interface (segregation thickness of 3 nm), and a slight depletion of Ba, Zr, and Ce is visible. These elemental mappings indicate the integration of Y and Ni cations into the perovskite structure near

the grain boundary, although the exact atomic positions cannot be determined. In the CONV sample, significant differences in grain boundary composition are evident. Ni forms a 5 nm thick grain boundary layer, while all other components - Ba, Zr, Ce, and Y - are significantly depleted at the interface. These two observations indicate a Ni-rich grain boundary film, which could be a remnant of the transient BaY_2NiO_5 phase formed during SSRS [19,20,24,68].

To further investigate the chemical composition of the grain boundaries in TPT1300, atom probe tomography (APT) was utilized in addition to electron microscopy. Figure 4c-4e presents a three-dimensional reconstruction from an APT analysis of a nanocrystalline TPT1300 sample, which includes an exemplary grain boundary proxigram. The data set displays two-grain boundaries near each other, with clear segregation of Y and Ni at the grain boundaries. Furthermore, slight variations in the composition are observed within grains, particularly for Ce. The composition of the interfaces shown in Fig. 4d-4e corroborates the findings previously revealed by STEM. The grain boundaries show significant segregation of Y and Ni and a decrease in Zr concentration from about 17.0 at% in bulk to about 14.2 at% at the interface due to the higher amount of Y and Ni accumulating at the interface. Although the strong curvature of grain boundaries in nanocrystalline microstructures causes slight broadening during data analysis, these results offer quantitative insight into the segregation behavior of Y and Ni at grain boundaries in TPT1300. The complete APT data set is provided in supplementary Fig. S7.

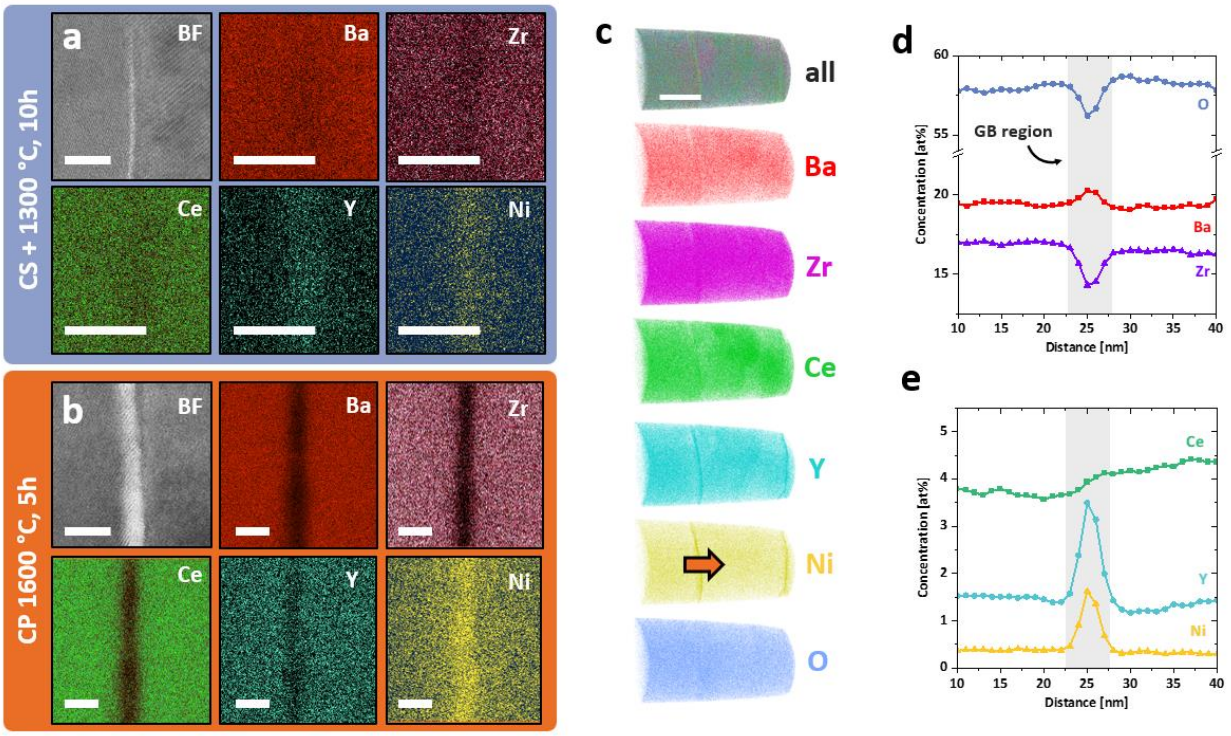

Figure 4: Grain boundary structure and chemistry of cs1300-BZCY ceramics. (a, b) BF-STEM micrographs and corresponding EDS maps of a grain boundary of TPT1300 (a) and CONV (b). Bright-field images in the top left corner exhibit significant structural differences between the two samples. Comparable observations can be made for the corresponding EDS mappings of the major components. The scale bars for BF and EDX are 5 nm. (c-e) APT investigation of grain boundaries in TPT1300. (c) APT atom maps illustrating the distribution of the main composition elements Ba, Zr, Ce, and Y, as well as the sintering aid Ni, with two interfaces visible in the Y and Ni atom maps. The APT scale bar is 50 nm. (d, e) Composition profiles (orange arrow in c) of a random grain boundary in TPT1300 were obtained to reveal the segregation behavior of Y and Ni to the grain boundary.

The detailed examination of the grain boundaries illustrates the different characteristics of the interfaces created by our novel process. A comparison with conventionally processed samples revealed significant differences in chemical composition and structure at the grain boundaries. The pre-densification step by cold sintering at 350 °C allows to achieve high relative densities at very low temperatures, removing the need to apply sintering temperatures over 1500 °C, which are required to reach sufficient densities by conventional processing. Subsequent thermal treatments

at intermediate temperatures bypass the formation of the transient BaY_2NiO_5 phase in conventional SSRS processing and prevent Ni-rich secondary phases from remaining at the grain boundary [18]. Instead, we process the cold-sintered samples at temperatures suitable to decompose residual $BaCO_3$ [56] and reform the perovskite phase by dissolving the precipitated Y-rich CeO_2 particles. The interdiffusion coefficients of Ce and Zr are sufficiently high at 1300 °C to form a single perovskite phase and allow equilibrium of the charged dopants at interface [69]. Bypassing the remaining transition phases at the grain boundaries allows Y and Ni to dissolve into the perovskite crystal structure and form a sharp segregation profile at the grain boundary. It is generally accepted that dopant segregation phenomena in oxide ceramics are driven by electrostatic and elastic driving forces that reduce the Gibbs free energy [70]. Dopants whose charge and ion size do not match the host lattice exhibit negative segregation energy toward surfaces [71,72] and grain boundaries [73]. In our case, both cases apply, i.e., the increased concentration of oxygen vacancies at the grain boundary core in $BaZrO_3$-based proton conductors [28,58,74] leads to a driving force for negatively charged point defects towards the grain boundary. Assuming that both Y and Ni are located at the B site of the perovskite (instead of Zr or Ce), both can be interpreted as negative point defects $Y'_{Zr/Ce}$ and $Ni''_{Zr/Ce}$, which are subjected to an electrostatic driving force toward the positively charged grain boundary core [75]. There, they can compensate for the core charge, reducing the magnitude of the space charge potential formed [35]. In addition to electrostatic effects, the cationic size mismatch between the host lattice (Zr^{4+}: 79 pm, Ce^{4+}: 103 pm) and the dopants (Y^{3+}: 93 pm and Ni^{2+}: 72 pm) leads to an additional elastic strain that drives segregation toward the interface.

Since the conduction path of protons in $BaZrO_3$-based ceramics is across the grain boundary rather than along it [28,57,76–80], the observed segregation behavior in cs1300-BZCY is considered to be the main reason for the high proton conductivities, despite low processing temperatures and very fine

microstructures. This allows us to overcome the blocking behavior of grain boundaries without applying SSRS or high-temperature annealing treatments, thus removing the main obstacle in lowering the sintering temperatures in BZCY ceramics. Another advantage of small grain size is the expected higher fracture strength, as usually observed in brittle ceramic materials[81], and previously confirmed for cold sintered ZnO[82]. Therefore, not only the ionic conductivity but also the mechanical reliability is enhanced by our novel approach.

4. Conclusions

This study introduces a novel low-temperature processing route for proton-conducting perovskites based on $BaZr_{0.7}Ce_{0.2}Y_{0.1}O_{3-\delta}$ (BZCY). A combination of cold sintering – a liquid and pressure-assisted technique – and suitable thermal post-treatments are used to fabricate dense, highly conductive BZCY electrolytes. Low-temperature densification through cold sintering is activated by the partial dissolution of Ce-rich components. An optimized thermal post-treatment (1300 °C, 10 h) can fully reform the perovskite phase after cold sintering, yielding stable, highly conductive, and dense BZCY ceramics.

Electrochemical characterization by impedance spectroscopy and DC measurements in all application-relevant atmospheres proves that low-temperature processed BZCY outperforms conventionally processed reference electrolytes sintered at 1600 °C. Furthermore, high protonic conductivity down to around 400 °C could be observed by measuring the isotopic effect in wet H_2 and D_2 atmospheres. The protonic conductivity in low-temperature processed BZCY is not limited by the grain boundary resistivity despite its nanograined microstructure. The high conductivity of grain boundaries can be associated with their pristine nature, a lack of residual Ni-rich secondary phases, and a high amount of segregated acceptor dopants. This allows to compensate parts of the

intrinsic core charge, reducing the blocking behavior of grain boundaries against the conduction of protons through the electrolyte.

The cold sintering pretreatment applied here deliberately changes the order between powder densification and final phase formation at the grain boundary, allowing us to bypass thermal regimes, which typically would lead to detrimental secondary phase formation and high interfacial resistances. Hereby, our novel sintering route solves one of the major obstacles in developing future ceramic proton conductors – the incompatibility between low sintering temperatures and high protonic conductivities [83] and provides optimal mechanical properties related to the fine microstructure. This novel processing strategy might open up new possibilities for grain boundary engineering and material combinations in proton-conducting ceramics, which were not possible beforehand due to the significant mismatch in required sintering temperatures.

Acknowledgment

The authors acknowledge Dr. Doris Sebold for help with SEM investigations and Dr. Yoo Jung Sohn for assistance with HT-XRD measurements. M.K. acknowledges financial support from the DFG under project number MA 1280/69-1. Additionally, D.J. and W.R. thank the DFG for funding within the Emmy Noether program (RH 146/1-1). A.V. expresses gratitude to Dr. Ivan Povstugar for his insightful discussions on the quality of APT data and its reconstruction. The authors thank Hitachi High-Technologies for providing access to the HF5000 STEM.

References

1. Serra, J. M. Electrifying chemistry with protonic cells. *Nat Energy* **4**, 178–179 (2019).
2. Yang, L. *et al.* Enhanced Sulfur and Coking Tolerance of a Mixed Ion Conductor for SOFCs: $BaZr_{0.1}Ce_{0.7}Y_{0.2-x}Yb_xO_{3-d}$. *Science (1979)* **326**, 126–129 (2009).
3. Duan, C. *et al.* Readily processed protonic ceramic fuel cells with high performance at low temperatures. *Science (1979)* **349**, 1321–1326 (2015).

4. Duan, C. *et al.* Highly durable, coking and sulfur tolerant, fuel-flexible protonic ceramic fuel cells. *Nature* **557**, 217–222 (2018).

5. Choi, S. *et al.* Exceptional power density and stability at intermediate temperatures in protonic ceramic fuel cells. *Nat Energy* **3**, 202–210 (2018).

6. Vøllestad, E. *et al.* Mixed proton and electron conducting double perovskite anodes for stable and efficient tubular proton ceramic electrolysers. *Nat Mater* **18**, 752–759 (2019).

7. An, H. *et al.* A 5 × 5 cm^2 protonic ceramic fuel cell with a power density of 1.3 W cm^{-2} at 600 °C. *Nat Energy* **3**, 870–875 (2018).

8. Deibert, W., Ivanova, M. E., Baumann, S., Guillon, O. & Meulenberg, W. A. Ion-conducting ceramic membrane reactors for high-temperature applications. *J Memb Sci* **543**, 79–97 (2017).

9. Kyriakou, V. *et al.* Methane steam reforming at low temperatures in a $BaZr_{0.7}Ce_{0.2}Y_{0.1}O_{2.9}$ proton conducting membrane reactor. *Appl Catal B* **186**, 1–9 (2016).

10. Malerød-Fjeld, H. *et al.* Thermo-electrochemical production of compressed hydrogen from methane with near-zero energy loss. *Nat Energy* **2**, 923–931 (2017).

11. Daniel, C. *et al.* Single-step hydrogen production from NH_3, CH_4, and biogas in stacked proton ceramic reactors. *Science (1979)* **376**, 390–393 (2022).

12. Ding, D. *et al.* A novel low-thermal-budget approach for the co-production of ethylene and hydrogen via the electrochemical non-oxidative deprotonation of ethane. *Energy Environ Sci* **11**, 1710–1716 (2018).

13. Ryu, K. H. & Haile, S. M. Chemical stability and proton conductivity of doped $BaCeO_3$–$BaZrO_3$ solid solutions. *Solid State Ion* **125**, 355–367 (1999).

14. Katahira, K., Kohchi, Y., Shimura, T. & Iwahara, H. Protonic conduction in Zr-substituted $BaCeO_3$. *Solid State Ion* **138**, 91–98 (2000).

15. Kreuer, K. D. Proton-Conducting Oxides. *Annu Rev Mater Res* **33**, 333–359 (2003).

16. Morejudo, S. H. *et al.* Direct conversion of methane to aromatics in a catalytic co-ionic membrane reactor. *Science (1979)* **353**, 563–566 (2016).

17. Robinson, S., Manerbino, A., Grover Coors, W. & Sullivan, N. P. Fabrication and performance of tubular, electrode-supported $BaCe_{0.2}Zr_{0.7}Y_{0.1}O_{3-\delta}$ fuel cells. *Fuel Cells* **13**, 584–591 (2013).

18. Tong, J., Clark, D., Bernau, L., Sanders, M. & O'Hayre, R. Solid-state reactive sintering mechanism for large-grained yttrium-doped barium zirconate proton conducting ceramics. *J Mater Chem* **20**, 6333–6341 (2010).

19. Tong, J., Clark, D., Bernau, L., Subramaniyan, A. & O'Hayre, R. Proton-conducting yttrium-doped barium cerate ceramics synthesized by a cost-effective solid-state reactive sintering method. *Solid State Ion* **181**, 1486–1498 (2010).

20. Nikodemski, S., Tong, J. & O'Hayre, R. Solid-state reactive sintering mechanism for proton conducting ceramics. *Solid State Ion* **253**, 201–210 (2013).

21. Babilo, P. & Haile, S. M. Enhanced sintering of yttrium-doped barium zirconate by addition of ZnO. *Journal of the American Ceramic Society* **88**, 2362–2368 (2005).

22. Ricote, S. & Bonanos, N. Enhanced sintering and conductivity study of cobalt or nickel doped solid solution of barium cerate and zirconate. *Solid State Ion* **181**, 694–700 (2010).

23. Ricote, S., Bonanos, N., Manerbino, A. & Coors, W. G. Conductivity study of dense $BaCe_xZr_{(0.9-x)}Y_{0.1}O_{(3-\delta)}$ prepared by solid state reactive sintering at 1500 °c. *Int J Hydrogen Energy* **37**, 7954–7961 (2012).

24. Huang, Y., Merkle, R. & Maier, J. Effects of NiO addition on sintering and proton uptake of $Ba(Zr,Ce,Y)O_{3-\delta}$. *J Mater Chem A Mater* **9**, 14775–14785 (2021).

25. Knight, M., Jennings, D., Ricote, S. & Reimanis, I. Estimating Ni valence with magnetometry in solid-state reactive sintered yttrium-doped barium zirconate. *Journal of the American Ceramic Society* **105**, 159–168 (2022).

26. Yamazaki, Y., Hernandez-Sanchez, R. & Haile, S. M. High total proton conductivity in large-grained yttrium-doped barium zirconate. *Chemistry of Materials* **21**, 2755–2762 (2009).

27. Cervera, R. B. *et al.* Structural study and proton transport of bulk nanograined Y-doped $BaZrO_3$ oxide protonics materials. *Solid State Ion* **179**, 236–242 (2008).

28. De Souza, R. A., Munir, Z. A., Kim, S. & Martin, M. Defect chemistry of grain boundaries in proton-conducting solid oxides. *Solid State Ion* **196**, 1–8 (2011).

29. Shirpour, M. *et al.* Dopant segregation and space charge effects in proton-conducting $BaZrO_3$ perovskites. *Journal of Physical Chemistry C* **116**, 2453–2461 (2012).

30. Shirpour, M., Merkle, R. & Maier, J. Evidence for space charge effects in Y-doped $BaZrO_3$ from reduction experiments. *Solid State Ion* **216**, 1–5 (2012).

31. Shirpour, M., Merkle, R., Lin, C. T. & Maier, J. Nonlinear electrical grain boundary properties in proton conducting Y-$BaZrO_3$ supporting the space charge depletion model. *Physical Chemistry Chemical Physics* **14**, 730–740 (2012).

32. Shirpour, M., Gregori, G., Houben, L., Merkle, R. & Maier, J. High spatially resolved cation concentration profile at the grain boundaries of Sc-doped $BaZrO_3$. *Solid State Ion* **262**, 860–864 (2014).

33. Clark, D. R. *et al.* Probing Grain-Boundary Chemistry and Electronic Structure in Proton-Conducting Oxides by Atom Probe Tomography. *Nano Lett* **16**, 6924–6930 (2016).

34. Vikrant, K. S. N., Rheinheimer, W. & Garcia, R. E. Electrochemical drag effect on grain boundary motion in ionic ceramics. *NPJ Comput Mater* **6**, 165-- (2020).

35. Shirpour, M., Merkle, R. & Maier, J. Space charge depletion in grain boundaries of $BaZrO_3$ proton conductors. *Solid State Ion* **225**, 304–307 (2012).

36. Dargatz, B., Gonzalez-Julian, J. & Guillon, O. Improved compaction of ZnO nano-powder triggered by the presence of acetate and its effect on sintering. *Sci Technol Adv Mater* **16**, 25008 (2015).

37. Funahashi, S. *et al.* Demonstration of the cold sintering process study for the densification and grain growth of ZnO ceramics. *Journal of the American Ceramic Society* **100**, 546–553 (2017).

38. Nur, K. *et al.* Influence of powder characteristics on cold sintering of nano-sized ZnO with density above 99 %. *J Eur Ceram Soc* **41**, 2648–2662 (2021).

39. Tsuji, K. *et al.* Single step densification of high permittivity $BaTiO_3$ ceramics at 300 ^oC. *J Eur Ceram Soc* **40**, 1280–1284 (2020).

40. Guo, N., Shen, H.-Z. & Shen, P. One-step synthesis and densification of $BaTiO_3$ by reactive cold sintering. *Scr Mater* **213**, 114628 (2022).

41. Zaengle, T. H. *et al.* Single-step densification of nanocrystalline CeO_2 by the cold sintering process. *Journal of the American Ceramic Society* **103**, 2979–2985 (2020).

42. Kabir, A. *et al.* Effect of cold sintering process (CSP) on the electro-chemo-mechanical properties of Gd-doped ceria (GDC). *J Eur Ceram Soc* **40**, 5612–5618 (2020).

43. Ohta, S. *et al.* Li^+ conducting garnet-type oxide sintering triggered by an H^+/Li^+ ion-exchange reaction. *J Mater Chem A Mater* **8**, 8989–8996 (2020).

44. Seo, J.-H. *et al.* Broad temperature dependence, high conductivity, and structure-property relations of cold sintering of LLZO-based composite electrolytes. *J Eur Ceram Soc* **40**, 6241–6248 (2020).

45. Guo, J. *et al.* Cold Sintering Process of Composites: Bridging the Processing Temperature Gap of Ceramic and Polymer Materials. *Adv Funct Mater* **26**, 7115–7121 (2016).

46. Guo, J. *et al.* Cold Sintered Ceramic Nanocomposites of 2D MXene and Zinc Oxide. *Advanced Materials* **30**, 1801846 (2018).

47. Si, M. *et al.* Preparation of Zinc Oxide/Poly-ether-ether-ketone (PEEK) Composites via the Cold Sintering Process. *Acta Mater* 117036 (2021) doi:https://doi.org/10.1016/j.actamat.2021.117036.

48. Sengul, M. Y., Guo, J., Randall, C. A. & van Duin, A. C. T. Water-Mediated Surface Diffusion Mechanism Enables the Cold Sintering Process: A Combined Computational and Experimental Study. *Angewandte Chemie International Edition* **58**, 12420–12424 (2019).

49. Guo, J. *et al.* Cold Sintering: A Paradigm Shift for Processing and Integration of Ceramics. *Angew Chem Int Ed Engl* **55**, 11457–11461 (2016).

50. Bouville, F. & Studart, A. R. Geologically-inspired strong bulk ceramics made with water at room temperature. *Nat Commun* **8**, 14655 (2017).

51. Gonzalez-Julian, J. *et al.* Unveiling the mechanisms of cold sintering of ZnO at 250 °C by varying applied stress and characterizing grain boundaries by Kelvin Probe Force Microscopy. *Acta Mater* **144**, 116–128 (2018).

52. Yan, N. *et al.* Discovery and Understanding of the Ambient-Condition Degradation of Doped Barium Cerate Proton-Conducting Perovskite Oxide in Solid Oxide Fuel Cells. *J Electrochem Soc* **162**, F1408 (2015).

53. Matsumoto, H., Kawasaki, Y., Ito, N., Enoki, M. & Ishihara, T. Relation Between Electrical Conductivity and Chemical Stability of $BaCeO_3$-Based Proton Conductors with Different Trivalent Dopants. *Electrochemical and Solid-State Letters* **10**, B77 (2007).

54. Kindelmann, M. *et al.* Cold sintering of $BaZr_{0.7}Ce_{0.2}Y_{0.1}O_{3-\delta}$ ceramics by controlling the phase composition of the starting powders. *Scr Mater* **224**, 115147 (2023).

55. Zhuravlev, Y. N. & Korabel'nikov, D. V. First-principle studies of the pressure effect on metal carbonates elastic properties. *Solid State Commun* **346**, 114706 (2022).

56. Arvanitidis, I., Siche, Du. & Seetharaman, S. A study of the thermal decomposition of $BaCO_3$. *Metallurgical and Materials Transactions B* **27**, 409–416 (1996).

57. Chen, C.-T., Danel, C. E. & Kim, S. On the origin of the blocking effect of grain-boundaries on proton transport in yttrium-doped barium zirconates. *J Mater Chem* **21**, 5435–5442 (2011).

58. Joakim Nyman, B., Helgee, E. E. & Wahnström, G. Oxygen vacancy segregation and space-charge effects in grain boundaries of dry and hydrated $BaZrO_3$. *Appl Phys Lett* **100**, 23–26 (2012).

59. Kreuer, K.-D., Fuchs, A. & Maier, J. HD isotope effect of proton conductivity and proton conduction mechanism in oxides. *Solid State Ion* **77**, 157–162 (1995).

60. Bonanos, N., Huijser, A. & Poulsen, F. W. H/D isotope effects in high temperature proton conductors. *Solid State Ion* **275**, 9–13 (2015).

61. Mather, G. C. *et al.* Phase Transitions, Chemical Expansion, and Deuteron Sites in the $BaZr_{0.7}Ce_{0.2}Y_{0.1}O_{3-\delta}$ Proton Conductor. *Chemistry of Materials* **28**, 4292–4299 (2016).

62. Simonenko, T. L. *et al.* Synthesis of $BaCe_{0.9-x}Zr_xY_{0.1}O_{3-\delta}$ nanopowders and the study of proton conductors fabricated on their basis by low-temperature spark plasma sintering. *Int J Hydrogen Energy* **44**, 20345–20354 (2019).

63. Wallis, J. *et al.* Structural and electrical properties of $BaZr_{0.7}Ce_{0.2}Y_{0.1}O_{3-\delta}$ proton conducting ceramic fabricated by spark plasma sintering. *Solid State Ion* **345**, 115118 (2020).

64. Wallis, J., Ricote, S., Weltmann, K. D., Burkel, E. & Kruth, A. The influence of the sintering temperature on $BaZr_{0.7}Ce_{0.2}Y_{0.1}O_{3-\delta}$ proton conductors prepared by Spark Plasma Sintering. *Ceram Int* **47**, 15349–15356 (2021).

65. Bu, J., Jönsson, P. G. & Zhao, Z. Dense and translucent $BaZr_xCe_{0.8-x}Y_{0.2}O_{3-\delta}$ (x = 0.5, 0.6, 0.7) proton conductors prepared by spark plasma sintering. *Scr Mater* **107**, 145–148 (2015).

66. Ricote, S., Bonanos, N. & Caboche, G. Water vapour solubility and conductivity study of the proton conductor $BaCe_{(0.9-x)}Zr_xY_{0.1}O_{(3-\delta)}$. *Solid State Ion* **180**, 990–997 (2009).

67. Gregori, G., Merkle, R. & Maier, J. Ion conduction and redistribution at grain boundaries in oxide systems. *Prog Mater Sci* **89**, 252–305 (2017).

68. Huang, Y., Merkle, R. & Maier, J. Effect of NiO addition on proton uptake of $BaZr_{1-x}Y_xO_{3-x/2}$ and $BaZr_{1-x}Sc_xO_{3-x/2}$ electrolytes. *Solid State Ion* **347**, (2020).

69. Hasle, I. *et al.* B-site cation inter-diffusion in yttrium substituted barium zirconate. *J Mater Chem A Mater* **9**, 21142–21150 (2021).

70. Wynblatt, P., Rohrer, G. S. & Papillon, F. Grain boundary segregation in oxide ceramics. *J Eur Ceram Soc* **23**, 2841–2848 (2003).

71. Lee, W., Han, J. W., Chen, Y., Cai, Z. & Yildiz, B. Cation Size Mismatch and Charge Interactions Drive Dopant Segregation at the Surfaces of Manganite Perovskites. *J Am Chem Soc* **135**, 7909–7925 (2013).

72. Kim, D., Bliem, R., Hess, F., Gallet, J.-J. & Yildiz, B. Electrochemical Polarization Dependence of the Elastic and Electrostatic Driving Forces to Aliovalent Dopant Segregation on $LaMnO_3$. *J Am Chem Soc* **142**, 3548–3563 (2020).

73. Yan, M. F., Cannon, R. M. & Bowen, H. K. Space charge, elastic field, and dipole contributions to equilibrium solute segregation at interfaces. *J Appl Phys* **54**, 764–778 (1983).

74. Helgee, E. E., Lindman, A. & Wahnström, G. Origin of space charge in grain boundaries of proton-conducting $BaZrO_3$. *Fuel Cells* **13**, 19–28 (2013).

75. Lindman, A., Bjørheim, T. S. & Wahnström, G. Defect segregation to grain boundaries in $BaZrO_3$ from first-principles free energy calculations. *J Mater Chem A Mater* **5**, 13421–13429 (2017).

76. Yang, Z., Woo, T. K., Baudin, M. & Hermansson, K. Atomic and electronic structure of unreduced and reduced CeO_2 surfaces: A first-principles study. *J Chem Phys* **120**, 7741–7749 (2004).

77. Iguchi, F., Sata, N., Tsurui, T. & Yugami, H. Microstructures and grain boundary conductivity of $BaZr_{1-x}Y_xO_3$ (x=0.05, 0.10, 0.15) ceramics. *Solid State Ion* **178**, 691–695 (2007).

78. Babilo, P., Uda, T. & Haile, S. M. Processing of yttrium-doped barium zirconate for high proton conductivity. *J Mater Res* **22**, 1322–1330 (2007).

79. Kjølseth, C. *et al.* Space-charge theory applied to the grain boundary impedance of proton conducting BaZr0.9Y0.1O3 - δ. *Solid State Ion* **181**, 268–275 (2010).

80. Iguchi, F., Sata, N. & Yugami, H. Proton transport properties at the grain boundary of barium zirconate based proton conductors for intermediate temperature operating SOFC. *J Mater Chem* **20**, 6265–6270 (2010).

81. Miyahara, N., Yamaishi, K., Mutoh, Y., Uematsu, K. & Inoue, M. Effect of Grain Size on Strength and Fracture Toughness in Alumina. *JSME international journal. Ser. A, Mechanics and material engineering* **37**, 231–237 (1994).

82. Nur, K. *et al.* Mechanical properties of cold sintered ZnO investigated by nanoindentation and micro-pillar testing. *J Eur Ceram Soc* **42**, 512–524 (2022).

83. Irvine, J. *et al.* Roadmap on inorganic perovskites for energy applications. *JPhys Energy* **3**, (2021).

84. Deibert, W. *et al.* Fabrication of multi-layered structures for proton conducting ceramic cells. *J Mater Chem A Mater* **3**, (2021).